




Cite this: *RSC Adv.*, 2025, 15, 8889

# Multifunctional copper–glutathione clusters with superior *p*-nitrophenol degradation and horseradish peroxidase-like activity†

Mayowa Oyebanji, Xuejiao Yang, Ling Chen, Wencai Sun, Ruru Qian, Haizhu Yu \* and Manzhou Zhu 

Copper nanoclusters (Cu NCs) are emerging as highly promising nanomaterials due to their unique physicochemical properties, making them an ideal platform for catalysis, sensing, and environmental remediation. This study explores the development of ultrasmall, water-soluble copper–glutathione (Cu–SG) nanoclusters, focusing on their catalytic capacity for the degradation of *p*-nitrophenol (*p*-NP), horseradish peroxidase (HRP)-like activity, and hydrogen peroxide (H<sub>2</sub>O<sub>2</sub>) detection. During synthesis, a combination of one-pot synthesis and acid-etching strategy was employed. The acid-etching approach was specifically utilized as an essential method to precisely regulate the structural properties of the clusters. The water-soluble ultrasmall Cu–SG nanoclusters show superior catalytic efficiency, achieving 98% conversion of *p*-NP to *p*-aminophenol (*p*-AP) within six minutes. The reaction followed first-order kinetics with a rate constant of 0.44 min<sup>−1</sup>, consistent with the Langmuir–Hinshelwood model. Notably, the Cu–SG retained catalytic efficiency across multiple reaction cycles, highlighting their recyclability and long-term stability. Additionally, Cu–SG exhibited excellent sensitivity and selectivity for rapid colorimetric H<sub>2</sub>O<sub>2</sub> detection due to the strong HRP-like activity, achieving a detection limit of 6.03 μM with high resistance to interference from other ions and compounds. Thermodynamic analysis demonstrates an enthalpy driven spontaneous reduction of *p*-NP with Cu–SG, wherein the van der Waals and hydrogen bonding interactions are predominant. By contrast, the interaction of Cu–SG with H<sub>2</sub>O<sub>2</sub> is an entropy-driven, spontaneous process, and the dominating hydrophobic forces drive the HRP-like catalytic mechanism. This study demonstrates the potential of the Cu–SG as an efficient, stable, and recyclable water-soluble copper nanocatalyst for pollutant degradation and as a sensitive sensor for reactive species.

Received 7th February 2025

Accepted 17th March 2025

DOI: 10.1039/d5ra00897b

rsc.li/rsc-advances

## 1. Introduction

Copper-based nanomaterials, particularly copper nanoclusters (Cu NCs), have attracted significant attention in recent years due to their unique properties, including high surface area, tunable optical characteristics, and remarkable catalytic activity. These properties make Cu NCs promising candidates for a wide range of applications, such as catalysis, sensing, and environmental remediation.<sup>1–4</sup> One of the most fascinating aspects of Cu NCs is their ability to undergo structural and electronic modifications in response to varying synthetic conditions.<sup>5–7</sup> A critical factor influencing the reactivity and

performance of Cu NCs is their surface chemistry, which is highly sensitive to the surrounding environment. Notably, acid-etching strategies can significantly affect their structural properties, leading to changes in stability, oxidation state, and reactivity.<sup>8–12</sup> Understanding the mechanisms underlying these reactions and exploring the effects of acid-etching on their physicochemical properties is important for optimizing the performance of Cu NCs across diverse applications.

In this study, we investigated the acid-etching approach in the transformation of copper–glutathione (Cu–SG) clusters, providing a comprehensive analysis on their synthesis, characterization, and potential applications in *p*-nitrophenol (*p*-NP) degradation, horseradish peroxidase (HRP)-like reactions, and hydrogen peroxide (H<sub>2</sub>O<sub>2</sub>) detection. Particular emphasis was placed on the influence of the acid-etching technique on Cu–SG clusters and the mechanisms underlying their catalytic activity. The structural properties of Cu–SG were systematically examined under increasingly acidic conditions to evaluate the effects on catalytic efficiency and sensor performance. After acid etching (pH = 2), Cu–SG demonstrated enhanced functionality,

Department of Chemistry and Centre for Atomic Engineering of Advanced Materials, Key Laboratory of Structure and Functional Regulation of Hybrid Materials of Physical Science and Information Technology, Anhui Province Key Laboratory of Chemistry for Inorganic/Organic Hybrid Functionalized Materials, Anhui University, Hefei 230601, China. E-mail: yuhaizhu@ahu.edu.cn

† Electronic supplementary information (ESI) available. See DOI: <https://doi.org/10.1039/d5ra00897b>



exhibiting excellent catalytic performance in the reduction of *p*-NP to *p*-aminophenol (*p*-AP) with high recyclability. Furthermore, its strong HRP-like activity enabled efficient colorimetric detection of H<sub>2</sub>O<sub>2</sub>, highlighting its potential as a versatile and practical candidate for real-world applications.

## 2. Experimental

### 2.1 Materials

All chemicals and reagents used in this study were purchased from Shanghai Macklin Biochemical Co., Ltd and used without further purification. These include: glutathione (GSH, 99%), Cu(NO<sub>3</sub>)<sub>2</sub> (AR), 3,3',5,5'-tetramethylbenzidine (TMB, 99%), H<sub>2</sub>O<sub>2</sub> (30%, AR), *p*-nitrophenol (*p*-NP, AR), 5,5-dimethyl-1-pyrroline-1-oxide (DMPO, 98%), 2,2,6,6-tetramethylpiperidin-1-oxyl (TEMP, 98%), Al(NO<sub>3</sub>)<sub>3</sub> (AR), KOH (AR), NaCl (AR), ZnCl<sub>2</sub> (99%), KCl (AR), fructose (98%), glucose (98%), sucrose (AR), ascorbic acid (98%), arginine (99%), histidine (99%), NaOH (AR), and HCl (AR). Before use, all glassware was thoroughly cleaned and dried in an oven. All solutions were prepared using Milli-Q ultrapure water as solvent.

### 2.2 Equipment

Transmission electron microscopy (TEM) and energy-dispersive spectroscopy (EDS) were conducted using a JEM-2100 microscope. Dynamic light scattering (DLS) analysis was performed with the Malvern Zetasizer ZS90. UV-visible absorption spectra were recorded on a Metash UV-9000PC spectrophotometer, and fluorescence spectra were obtained using the HORIBA FluoroMax-4P fluorescence spectrophotometer. Fourier-transform infrared (FT-IR) spectroscopy was performed on a Bruker Vertex80+ Hyperion spectrometer. X-ray photoelectron spectroscopy (XPS) measurements were carried out using an ESCALAB 250 spectrometer with monochromated Al K $\alpha$  radiation. Electron paramagnetic resonance (EPR) spectroscopy was performed on a Magnettech ESR 5000 spectrometer. The electrochemical measurements were carried out on a CHI 660E electrochemical workstation (CHI Instruments) with a three-electrode system. The working electrode was a glassy carbon, an Ag/AgCl was used as the reference electrode, and a Pt wire was used as the counter electrode in PBS buffer at room temperature. Before the testing, the sample solution was degassed with a high-purity N<sub>2</sub> gas.

### 2.3 Synthesis of Cu-SG

The Cu-SG clusters were synthesized through a one-pot chemical reduction process combined with an acid-etching strategy. Briefly, 0.8 mL of 200 mM glutathione (GSH) was added to 18.4 mL of ultrapure water. Subsequently, 0.4 mL of 100 mM Cu(NO<sub>3</sub>)<sub>2</sub> solution was introduced, and the mixture was stirred for 10 minutes, resulting in a turbid solution. The pH of the solution was adjusted to 10 by the dropwise addition of 3 M NaOH, which caused the solution to turn clear. The mixture was then heated in a water bath at 80 °C with continuous stirring for 6 hours. After cooling to room temperature, the acid-etching process was performed by gradually adding 1 M HCl, with the

effects studied progressively until the solution reaches to pH = 2. For clarity, the intermediate state prior to the acid etching was designated as the copper nanoparticles (Cu-NPs) for its relatively larger size (Fig. S1†). Unless otherwise specified, the Cu-SG clusters formed under pH = 2 condition were used in the following tests, and the samples were stored in dark at 4 °C for further experiments.

### 2.4 Catalytic performance for *p*-NP degradation and recycling of the Cu-SG

For the *p*-NP degradation experiments, 300  $\mu$ L of freshly prepared 200 mM NaBH<sub>4</sub> was added to 3 mL of 100  $\mu$ M *p*-NP solution, followed by the addition of 50  $\mu$ L of Cu-SG. The reaction progress was monitored using UV-vis spectroscopy by measuring absorbance at characteristic wavelengths: 317 nm for *p*-NP, 400 nm for *p*-nitrophenolate, and  $\sim$ 295 nm for *p*-AP. The reaction kinetics are consistent with the equation<sup>13,14</sup>

$$-\ln(C_t/C_0) = -\ln(A_t/A_0) = kt$$

where  $C_0$  and  $C_t$  represent the concentration of *p*-NP at times 0 and  $t$ ;  $A_0$  and  $A_t$  represent the UV/vis absorbance (at 400 nm) of *p*-NP at times 0 and  $t$ , respectively, and  $k$  represents the apparent rate constant (min<sup>-1</sup>). For catalyst recycling, the Cu-SG clusters were recovered by filtration through an ultrafilter (MWCO = 3000), followed by washing with ultrapure water adjusted to pH 2 prior to reuse.

### 2.5 HRP-like kinetic analysis of Cu-SG

The HRP-like activity of Cu-SG was analyzed through steady-state kinetics. Using H<sub>2</sub>O<sub>2</sub> and TMB as substrates, measurements were conducted by varying the concentration of one substrate while keeping the other constant. The absorbance of oxidized TMB (TMB<sub>ox</sub>) at 652 nm was recorded using UV-vis spectroscopy. For the assay, 100  $\mu$ L of Cu-SG was mixed with 100  $\mu$ L of H<sub>2</sub>O<sub>2</sub> at varying concentrations (5–100 mM) and 100  $\mu$ L of TMB (10 mM). Alternatively, 100  $\mu$ L of TMB at different concentrations (8–20 mM) was mixed with 100  $\mu$ L of H<sub>2</sub>O<sub>2</sub> (60 mM). The reaction mixture was adjusted to a total volume of 2 mL and incubated at ambient temperature for 20 minutes before spectrophotometric analysis. The enzymatic reaction kinetic constants ( $v_{\max}$ ,  $K_m$ ) were calculated using the Michaelis–Menten equation:

$$v = C \cdot v_{\max} / K_m + C$$

where  $v$  is the initial reaction velocity,  $v_{\max}$  is the maximal reaction velocity,  $C$  is the concentration of substrate, and  $K_m$  is the apparent Michaelis–Menten constant. The linearity of the data was examined using Lineweaver–Burk plots, derived from the double reciprocal of the Michaelis–Menten equation.<sup>12,15,16</sup>

### 2.6 Selective colorimetric analysis of H<sub>2</sub>O<sub>2</sub> with Cu-SG

For the quantitative colorimetric analysis of H<sub>2</sub>O<sub>2</sub>, 100  $\mu$ L of freshly prepared H<sub>2</sub>O<sub>2</sub> solutions at various concentrations (0–1250  $\mu$ M) were mixed with 100  $\mu$ L of 10 mM TMB and 100  $\mu$ L of



Cu-SG. The total volume was adjusted to 2 mL with ultrapure water, and the reaction mixture was incubated at room temperature for 20 minutes before spectrophotometric analysis. The absorbance of TMB<sub>ox</sub> was monitored at 652 nm using UV-vis spectroscopy. To assess the selectivity of the Cu-SG-based probe, interference tests were conducted by replacing H<sub>2</sub>O<sub>2</sub> with 100  $\mu$ L of 2000  $\mu$ M solutions of various ions and compounds, including Al(NO<sub>3</sub>)<sub>3</sub>-Al<sup>3+</sup>, KOH-K<sup>+</sup>, NaCl-Na<sup>+</sup>, ZnCl<sub>2</sub>-Zn<sup>2+</sup>, KCl-Cl<sup>-</sup>, fructose (Fru.), glucose (Glu.), sucrose (Suc.), ascorbic acid (AA), arginine (Arg.), histidine (His.), and GSH into the detection solution. The results were evaluated by comparing the absorbance changes under the same experimental conditions.

### 3. Results and discussion

#### 3.1 Characterization of the Cu-SG

The elemental analysis of Cu-NPs (the intermediate states prior to the acid-etching) by EDS demonstrates the successful incorporation of GSH in the particles (Fig. S2†). Then the acid-etching process induced characteristic changes in the size and properties of the Cu-NPs. TEM and DLS analysis (Fig. 1 and S1†) revealed a progressive reduction in particle size and improved dispersion with increasing acidity. Under highly acidic conditions (pH = 2), the Cu-SG clusters exhibited a uniform, mono-dispersed size distribution, ranging from 0.4 to 1.8 nm with an average size of  $\sim$ 1 nm (Fig. 1a inset) according to TEM analysis, which is comparable to the DLS results ranging from 0.5 to 1.9 nm with an average size of  $\sim$ 1.12 nm (Fig. 1b).

UV-vis spectrometry was further employed to investigate the optical absorption properties of the Cu-SG system during acid-etching and to correlate the results with TEM and DLS analyses. The UV-vis spectra (Fig. 2a and S3a†) supported the TEM and DLS findings, showing that the Cu-SG solution in a strongly acidic environment exhibited peaks exclusively below 400 nm, characteristic of copper nanoclusters (Cu NCs).<sup>17–20</sup> Notably, an additional shoulder peak at  $\sim$ 290 nm confirmed the formation of ultra-small Cu NCs. In contrast, under increasingly alkaline conditions, the Cu-SG solution displayed optical features indicative of larger Cu-NPs, evidenced by a surface plasmon

resonance (SPR) peak at approximately 620 nm (Fig. S3a†).<sup>21,22</sup> Fluorescence analysis further underscored the effects of acid-etching on the optical properties of Cu-SG. The fluorescence emission spectra (Fig. 2a) revealed dual fluorescence features with emission peaks at 430 nm and 505 nm under strongly acidic conditions. In comparison, the Cu-NPs system in alkaline environment exhibited a single fluorescence peak at 430 nm (Fig. S3b†). This distinct fluorescence behavior highlights the significant influence of acid-etching on the optical properties of the Cu-SG system.

Following the optical investigations, FT-IR spectroscopy was analyzed to identify the characteristic functional groups in both pure GSH and Cu-SG (Fig. 2b). The FT-IR spectrum of pure GSH exhibited distinct peaks, including O-H stretching at 3344 cm<sup>-1</sup>, N-H stretching at 3247 cm<sup>-1</sup>, and asymmetric and symmetric N-H stretches at 3129 cm<sup>-1</sup> and 3028 cm<sup>-1</sup>, respectively. Additional features included an S-H stretching band at 2524 cm<sup>-1</sup>, a C=O stretching band at 1718 cm<sup>-1</sup>, and amide I and amide II vibrations at 1624 cm<sup>-1</sup> and 1546 cm<sup>-1</sup>, respectively. Peaks corresponding to the asymmetric and symmetric COO<sup>-</sup> vibrations appeared at 1584 cm<sup>-1</sup> and 1394 cm<sup>-1</sup>, respectively.<sup>23–25</sup> After coordination with copper, most peaks were maintained, indicating the largely preserved structure of ligand in the formed clusters. However, the characteristic S-H stretching band of GSH was absent in all samples during acid etching, implying the possible coordination of the thiol group in GSH with copper, and thus the formation of Cu-S bonds.<sup>26</sup> Meanwhile, the broadened N-H and C=O peaks demonstrate the complicated chemical environment of the amide and carboxylic groups.<sup>27</sup>

To probe the oxidation state of Cu-SG, X-ray photoelectron spectroscopy (XPS) analysis was performed, providing detailed insights into the chemical states present. The XPS full-spectrum survey of Cu-SG revealed characteristic peaks at 167.7 eV (S 2p), 198.1 eV (Cl 2p), 285.0 eV (C 1s), 400.0 eV (N 1s), 531.8 eV (O 1s), and 1071.0 eV (Na 1s) (Fig. S5a†).<sup>26</sup> These peaks corresponded to the expected components of the GSH ligands used in synthesis, confirming the successful integration of copper with the ligands. To further examine the oxidation state of copper, high-resolution XPS spectra were recorded for the Cu 2p region. Two

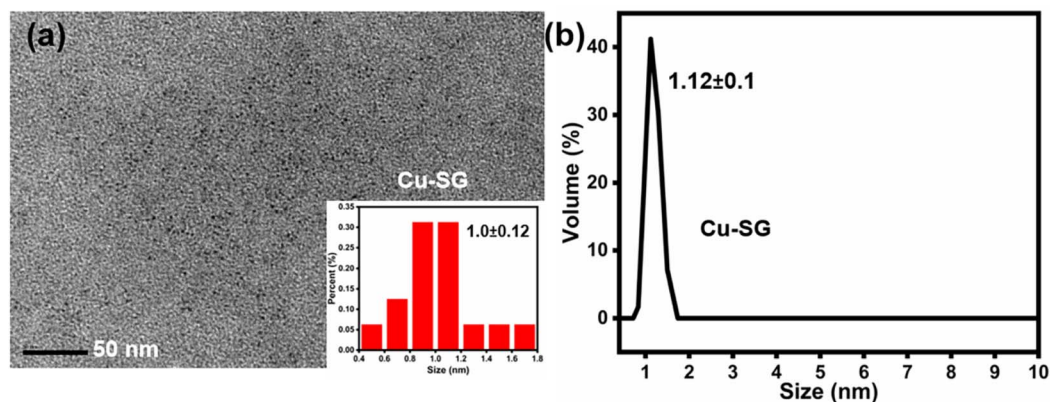


Fig. 1 (a) TEM image (inset: size distribution of Cu-SG); and (b) DLS results of Cu-SG.

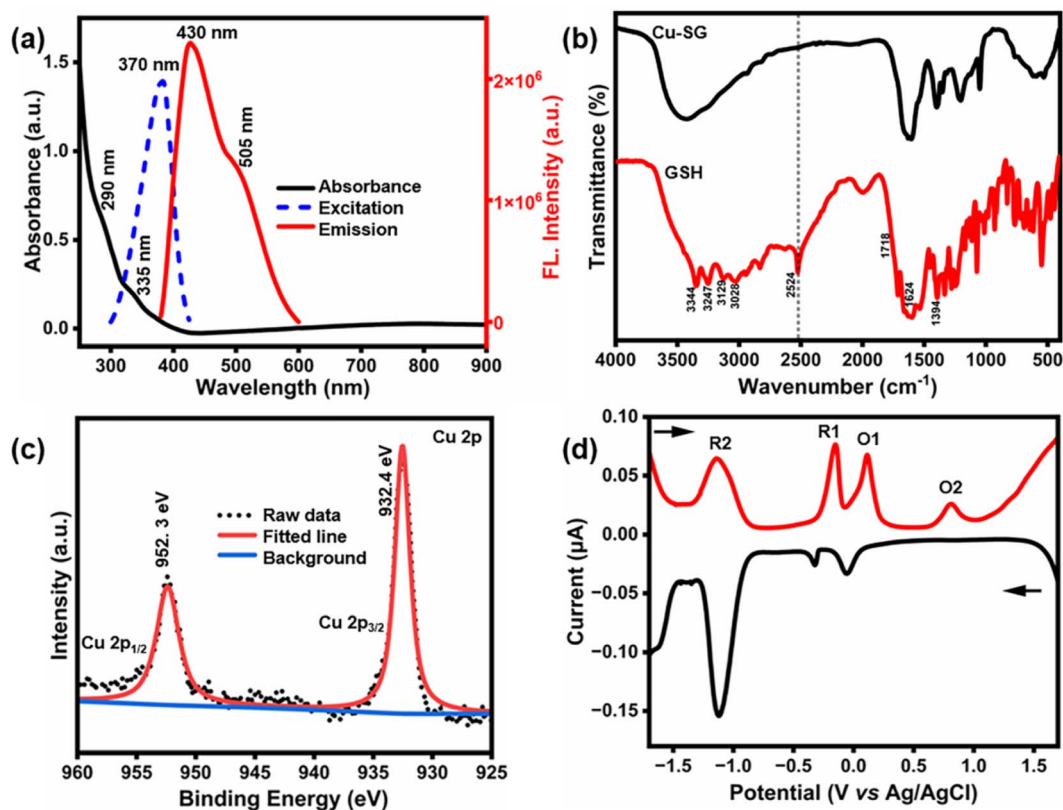


Fig. 2 (a) UV-vis absorption (black line), fluorescence excitation (blue dash line) and emission curves (red line, upon excitation at 370 nm) of Cu-SG; (b) FT-IR spectra of GSH and Cu-SG; (c) XPS spectra in the Cu 2p region of Cu-SG; and (d) DPV curve of Cu-SG.

prominent peaks were observed at 952.3 eV and 932.4 eV, corresponding to the Cu 2p<sub>1/2</sub> and Cu 2p<sub>3/2</sub> energy levels, respectively (Fig. 2c). These peaks persisted across the Cu-SG system during acid-etching processes, though they exhibited shifts toward lower binding energies as the acid-etching intensity increased (Fig. S5b†), such shifts are attributed to potential changes in quantum size, surface charge, and electron density redistribution.<sup>28–30</sup> The absence of the satellite peak at ~942 eV in XPS excludes the possibility of Cu(II).<sup>31,32</sup> Meanwhile, The DPV curves of Cu-SG (Fig. 2d) displayed distinct reduction (R1, -0.14 V) and oxidation (O1, 0.12 V) peaks. The small O1 and R1 values highlight the potential of Cu-SG to participate in redox reactions, as later demonstrated in *p*-NP reduction and TMB oxidation experiments.

### 3.2 Catalytic degradation of *p*-NP with Cu-SG

The catalytic potential of Cu-SG was investigated in the NaBH<sub>4</sub>-assisted reduction of *p*-NP. *p*-NP is a common industrial pollutant that raises significant environmental and health concerns due to its toxicity and persistence in aquatic systems.<sup>33–35</sup> Its reduction to *p*-AP, a valuable precursor for pharmaceuticals and dyes, not only serves to remove a hazardous compound but also produces a useful chemical.<sup>13,14,36</sup> A widely used approach for *p*-NP degradation involves NaBH<sub>4</sub> as a reductant, in conjunction with a catalyst.<sup>36–39</sup> In this study, the redox activity of Cu-SG enabled its use as an efficient

catalyst to facilitate the reduction of *p*-NP to *p*-AP (Scheme S1†). The UV-vis absorption spectra were used to monitor the reduction reaction. Initially, the *p*-NP solution exhibited a maximum absorption peak at 317 nm. Upon the addition of NaBH<sub>4</sub>, the solution turned bright yellow due to the formation of 4-nitrophenolate anions, characterized by a new peak at 400 nm. In the absence of the Cu-SG catalyst, the absorption peak at 400 nm remained unchanged even after 48 hours, indicating no progression in the reduction reaction (Fig. 3a).

Upon the addition of Cu-SG as the catalyst, the absorption peak at 400 nm rapidly disappeared within 6 minutes, and the bright yellow solution turned colorless (Fig. 3b). This rapid change highlighted the catalytic efficiency of Cu-SG in the degradation process. By contrast, the Cu cluster samples gained by the acid etching under otherwise pH conditions all show no catalytic activity (Fig. S6 and Table S1†). Furthermore, using an ultrafiltration (MWCO 3000 kD) strategy, the Cu-SG catalyst could be easily recycled and reused for over five cycles (>90% conversion for each cycle, Fig. 3c). DLS analysis indicates the maintained cluster size of Cu-SG before and after the *p*-NP reduction (Fig. S7†). These results, and especially the recyclable characteristics underscore the practical potential of Cu-SG as a stable and recyclable nanocatalyst for environmental pollutant remediation.

The reaction kinetics and degradation pathway of *p*-NP are presented by plotting  $-\ln(C_t/C_0)$  against time (*t*) (Fig. 3d),





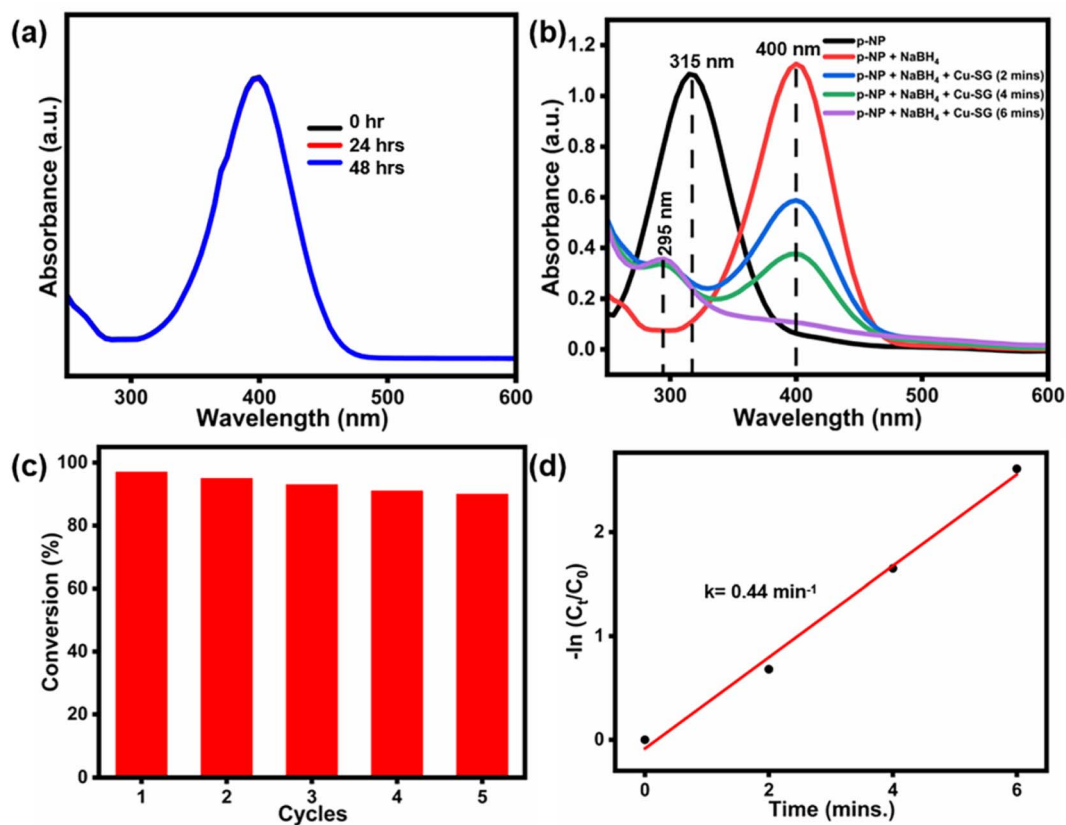
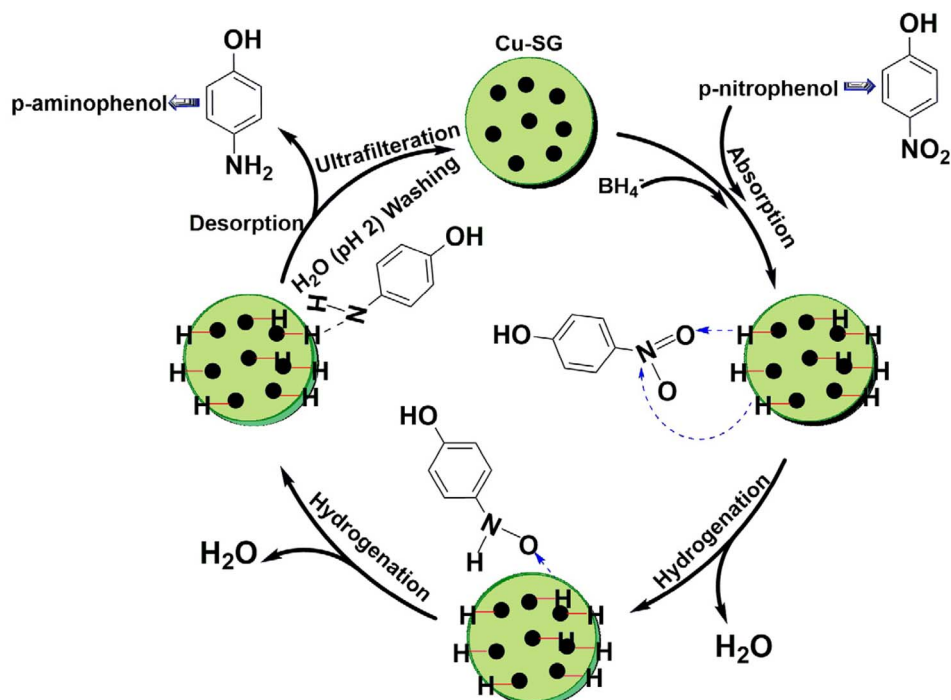


Fig. 3 (a) The optical absorption spectra of *p*-NP + NaBH<sub>4</sub> in the absence of Cu-SG at different time point; (b) time-dependent optical absorption spectra of *p*-NP reduction by Cu-SG; (c) reusability of the Cu-SG for the catalytic reduction of *p*-NP. Conversions were calculated from the UV-vis absorption spectra; and (d) linear fitting of the reaction rate constant.



Scheme 1 The proposed *p*-NP degradation pathway catalyzed by Cu-SG.

which reveals a quasi-linear relationship. This suggests that the degradation follows a first-order rate law, with a rate constant ( $k$ ) of  $0.44 \text{ min}^{-1}$ . Such behavior is consistent with the Langmuir–Hinshelwood model.<sup>13,14</sup> In this model, the reaction takes place on the surface of the catalyst, with the adsorption of reactants playing a crucial role in determining the overall rate. The reaction rate is therefore governed by the concentration of the adsorbed species. This suggests that the reaction pathway for the Cu-SG-catalyzed reduction of *p*-NP to *p*-AP (Scheme 1) begins with the synergistic adsorption of both *p*-NP and the hydrogen donor  $\text{NaBH}_4$  onto the Cu-SG surface. The reaction proceeds through a series of hydrogenation steps, where *p*-NP is progressively reduced, ultimately yielding *p*-AP.

### 3.3. HRP-like activity of Cu-SG

Motivated by capacity of Cu-SG in regulating electron transfer, we further analyzed the biomimetic activity of Cu-SG, mainly focusing on the HRP-like activity of Cu-SG.<sup>40–42</sup> TMB was used as a molecular probe in this series of tests. In the presence of  $\text{H}_2\text{O}_2$ , Cu-SG catalyzed the conversion of the colorless TMB to blue  $\text{TMB}_{\text{ox}}$  (Fig. 4a). The optimal HRP-like activity of Cu-SG was observed with increased acidity (Fig. S8†).

The kinetic mechanism of Cu-SG was assessed using enzyme kinetics, and typical Michaelis–Menten curves (Fig. 4b and c)

were obtained and fitted well (Fig. 4b and c, insets).<sup>12,40,43,44</sup> The Michaelis constant ( $K_m$ ) and maximal reaction velocity ( $V_{\text{max}}$ ) of Cu-SG with respect to  $\text{H}_2\text{O}_2$  ( $K_m = 0.4133 \text{ mM}$ ,  $V_{\text{max}} = 1.50 \times 10^{-7} \text{ m s}^{-1}$ ) and TMB ( $K_m = 2.1099 \text{ mM}$ ,  $V_{\text{max}} = 1.21 \times 10^{-7} \text{ m s}^{-1}$ ) are among the first-level HRP-like nanomaterials (Table S2†), and relatively higher than those of the nature HRP. The results suggest that Cu-SG exhibits stronger affinities and efficient catalytic kinetics toward both substrates. Furthermore, the excellent linearity of the double-reciprocal plots of the substrates suggests a double-displacement (Ping-Pong) mechanism, typical for HRP and similar nanomaterials.<sup>45,46</sup> Of note, the HRP-like activity of Cu-SG remains stable even after storage for about two months, indicating its excellent long-term stability (Fig. 4d).

To confirm that the reaction mechanism follows the “Ping-Pong” model, the type of the primary reactive oxygen species ( $\cdot\text{OH}$ ,  $\cdot\text{O}_2^-$ , and  $^1\text{O}_2$ , abbreviated as ROS) were investigated, as they play an important role in the chromogenic reaction in the presence of  $\text{H}_2\text{O}_2$ .<sup>41,42,47</sup> EPR analysis was performed with DMPO and TEMP as radical trappers, and the characteristic EPR signals attributing to  $\text{DMPO}\cdot\text{O}_2^-$  (Fig. 5a)<sup>48–51</sup> and  $\text{TEMP}\cdot^1\text{O}_2$  (Fig. 5b) were observed.<sup>50–52</sup> Based on these findings, the HRP-like reaction mechanism of Cu-SG starts with the decomposition of  $\text{H}_2\text{O}_2$  into  $\cdot\text{O}_2^-$  and  $^1\text{O}_2$ , and then the oxidation of TMB.<sup>53–55</sup>

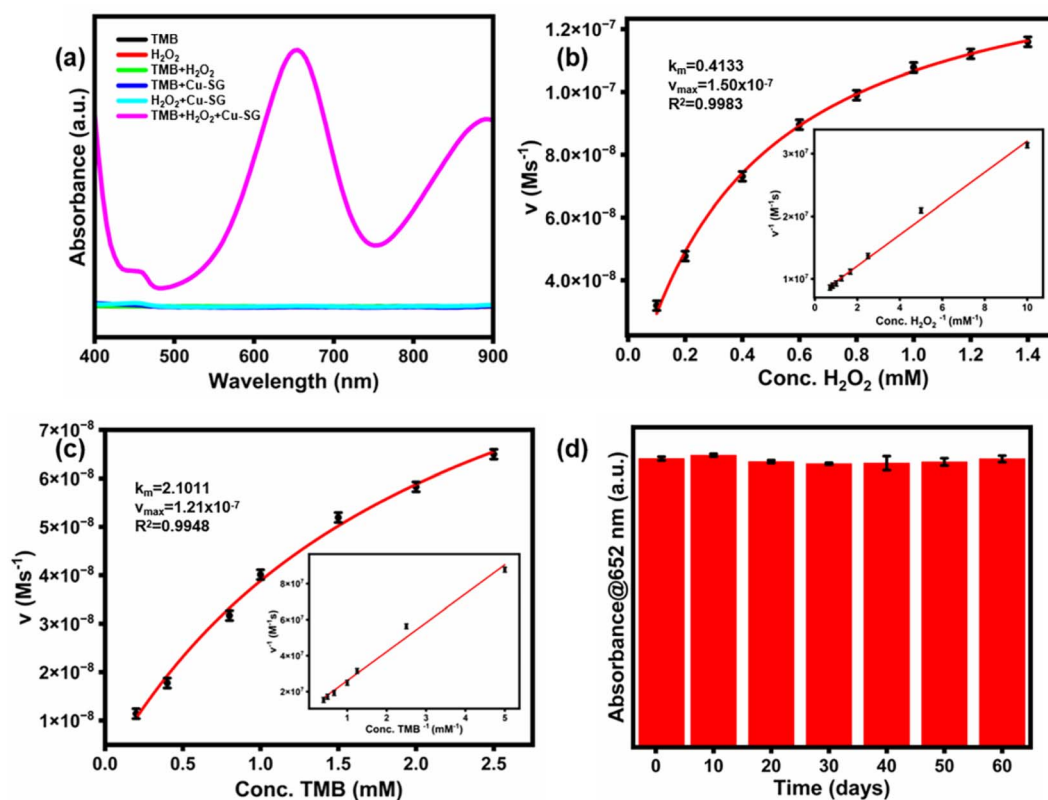


Fig. 4 (a) The UV-vis absorption spectra of the different reaction systems; steady-state kinetic assay of Cu-SG: (b) with the concentration of TMB at 10 mM; (c) with the concentration of  $\text{H}_2\text{O}_2$  at 60 mM (insets: Lineweaver–Burk plots of the double reciprocal of the Michaelis–Menten equation) (d) long-term stability study of the Cu-SG solution stored at 4 °C via testing the optical absorption at 652 nm for the (Cu-SG +  $\text{H}_2\text{O}_2$  + TMB) system.



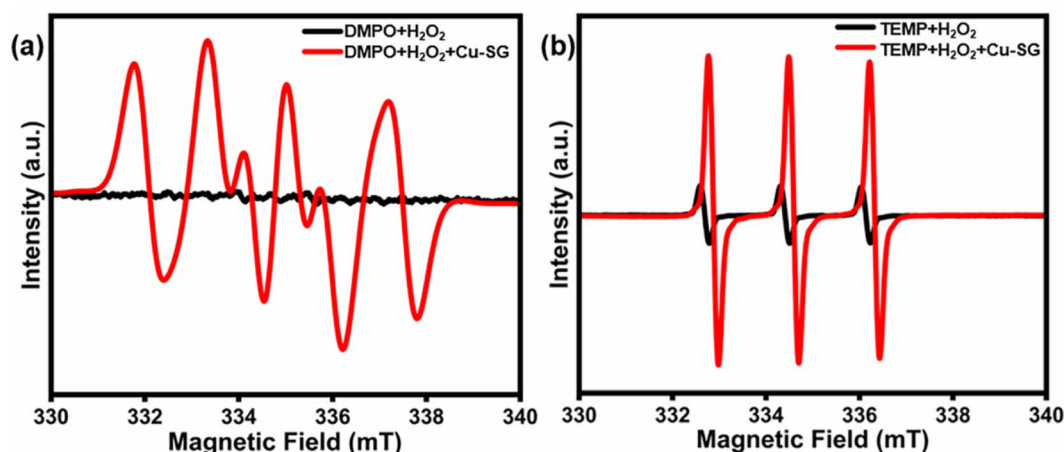


Fig. 5 EPR spectra of (a) H<sub>2</sub>O<sub>2</sub>/DMPO with Cu-SG; and (b) H<sub>2</sub>O<sub>2</sub>/TEMP with Cu-SG.

### 3.4 Quantitative colorimetric H<sub>2</sub>O<sub>2</sub> detection

The detection of H<sub>2</sub>O<sub>2</sub> is of importance in various fields, including environmental monitoring, clinical diagnostics, and industrial processes.<sup>56,57</sup> Due to its high reactivity and oxidative power, H<sub>2</sub>O<sub>2</sub> plays an essential role in many chemical processes,

but its concentration must be carefully monitored because of its potential toxicity. To address this, several sensor systems based on nanomaterials have been developed for rapid and sensitive H<sub>2</sub>O<sub>2</sub> detection<sup>58–60</sup> Inspired by the HRP-like properties and ROS-generating ability of Cu-SG, the quantitative detection of

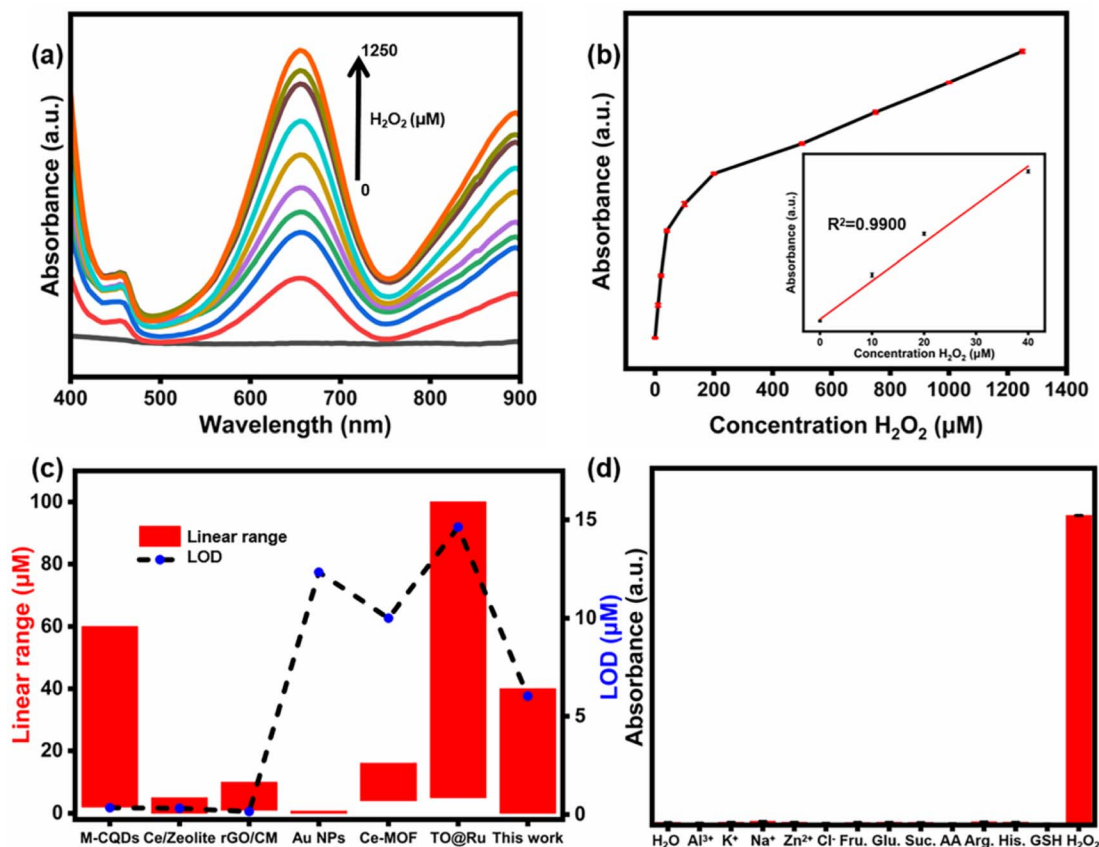


Fig. 6 (a) UV-vis absorption analysis of H<sub>2</sub>O<sub>2</sub> (0, 10, 20, 40, 100, 200, 500, 750, 1000, and 1250 μM) in presence of Cu-SG and TMB (b) linear correlation of optical absorption intensity vs. H<sub>2</sub>O<sub>2</sub> concentrations. (inset is the linear range from 0 to 40 μM); (c) comparison of the linear range and LOD of Cu-SG with those of other HRP-like nanomaterials for H<sub>2</sub>O<sub>2</sub> detection; and (d) selectivity assessment of the Cu-SG probe for H<sub>2</sub>O<sub>2</sub> detection (500 μM) and interference (2000 μM).

H<sub>2</sub>O<sub>2</sub> was investigated using a colorimetric approach. The absorbance at 652 nm increased gradually with the concentration of H<sub>2</sub>O<sub>2</sub> in the presence of Cu-SG and TMB (Fig. 6a). A strong linear correlation between absorbance at 652 nm and H<sub>2</sub>O<sub>2</sub> concentration (0–1250 μM) was observed (Fig. 6b), with excellent linearity within the narrow range of 0 to 40 μM (correlation value = 0.9900, inset of Fig. 6b). The linear range and LOD of Cu-SG were comparable to those of the recently reported HRP-like nanomaterials (Fig. 6c and Table S3†). The limit of detection (LOD) was determined to be 6.03 μM (based on 3σ/S).

The selectivity and sensitivity of the Cu-SG probe towards H<sub>2</sub>O<sub>2</sub> were evaluated by testing its response to potential interfering ions and compounds (with 3-fold higher concentration than that of H<sub>2</sub>O<sub>2</sub>) under otherwise identical conditions. As shown in Fig. 6d, these interfering species had negligible impact on the UV-vis absorption response of the Cu-SG-TMB probe in the H<sub>2</sub>O<sub>2</sub>-sensing system, demonstrating the high specificity of the Cu-SG probe for H<sub>2</sub>O<sub>2</sub> detection in complex matrices.

### 3.5 Thermodynamic studies

Herein, fluorescence analysis has been conducted at three different temperatures (298, 303, and 308 K) to examine the influence of standard conditions on the reaction pathways for Cu-SG with *p*-NP or H<sub>2</sub>O<sub>2</sub> (Fig. S9†), on the basis of the Stern-Volmer equation eqn (1)<sup>61,62</sup>

$$F_0/F = 1 + K_{sv}[C] \quad (1)$$

$F_0$  and  $F$  represent the fluorescence intensities of Cu-SG in the absence and presence of *p*-NP, respectively,  $K_{sv}$  is the Stern-Volmer constant, and  $[C]$  denotes the analyte concentration.

The Stern-Volmer plot for the Cu-SG-*p*-NP system presented in Fig. 7a and the linearity indicates a quantitative 1 : 1 binding. On this base, the binding constant ( $K_a$ ) was calculated according to the logarithmic relationship of eqn (2).<sup>63,64</sup>

$$\log[(F_0 - F)/F] = \log K_a + \log[C] \quad (2)$$

The temperature dependence of the binding constants was examined at 298, 303, and 308 K (Table 1), as this range is generally considered to minimize significant structural or

**Table 1** Thermodynamic parameters for Cu-SG upon interaction with *p*-NP and H<sub>2</sub>O<sub>2</sub>

System	<i>T</i> (K)	<i>K<sub>a</sub></i> (M <sup>−1</sup> )	Δ <i>G</i> <sup>0</sup> (kJ mol <sup>−1</sup> )	Δ <i>H</i> <sup>0</sup> (kJ mol <sup>−1</sup> )	Δ <i>S</i> <sup>0</sup> (J mol <sup>−1</sup> K <sup>−1</sup> )
<i>p</i> -NP	298	1.48 × 10 <sup>3</sup>	−18.28	−169.08	−506.02
	303	6.12 × 10 <sup>2</sup>	−15.75		
	308	1.61 × 10 <sup>2</sup>	−13.22		
H <sub>2</sub> O <sub>2</sub>	298	1.22 × 10 <sup>2</sup>	−11.98	44.73	190.29
	303	1.81 × 10 <sup>2</sup>	−12.93		
	308	2.19 × 10 <sup>2</sup>	−13.88		

conformational changes in the reaction system.<sup>65</sup> This assumption allows the estimation of Δ*H*<sup>0</sup> and Δ*S*<sup>0</sup> values using the Van't Hoff equation eqn (3)

$$\ln K_a = -\Delta H^0/RT + \Delta S^0/R \quad (3)$$

where  $R$  is the gas constant, and  $T$  is the temperature. The Van't Hoff plot of  $\ln K_a$  against  $T^{-1}$  (Fig. 7c) allowed the estimation of Δ*H*<sup>0</sup> and Δ*S*<sup>0</sup> from the slope and intercept, and thus the Δ*G*<sup>0</sup> could be deduced accordingly *via* eqn (4)

$$\Delta G^0 = \Delta H^0 - T\Delta S^0 \quad (4)$$

According to the results in Table 1, the Δ*G*<sup>0</sup> < 0, Δ*H*<sup>0</sup> < 0, and Δ*S*<sup>0</sup> < 0 indicate an exergonic interaction under ambient conditions, suggesting the dominance of van der Waals and hydrogen bonding interactions among Cu-SG and *p*-NP.<sup>61,62</sup> The results indicates the strong interaction of Cu-SG with *p*-NP, which might drive the subsequent reduction of *p*-NP *via* reacting with NaBH<sub>4</sub>.

Similar to aforementioned procedures, the interaction of Cu-SG with H<sub>2</sub>O<sub>2</sub> was also investigated, while a modified Stern-Volmer equation eqn (5) was first applied to account to the enhanced luminescence:

$$F/F_0 = 1 + K_{sv}[C] \quad (5)$$

On the basis of the Stern-Volmer plots (Fig. 7b) and thermodynamic values gained from the Van't Hoff equation, Δ*G*<sup>0</sup> < 0 with Δ*H*<sup>0</sup> > 0 and Δ*S*<sup>0</sup> > 0 indicates that the Cu-SG and H<sub>2</sub>O<sub>2</sub> interaction is endothermic but exergonic, suggesting the dominance of hydrophobic forces.

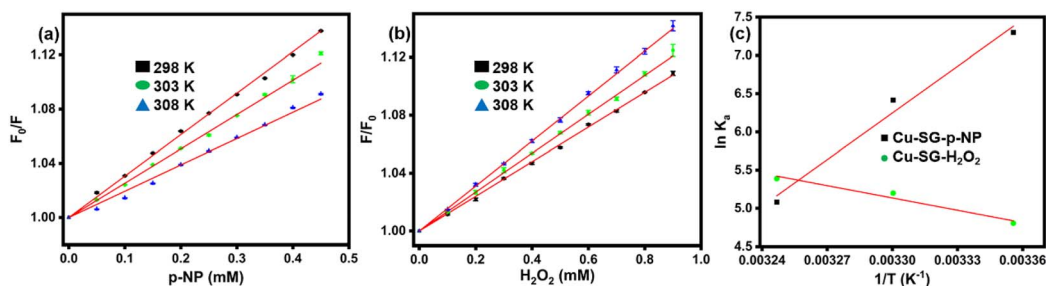


**Fig. 7** The derived Stern-Volmer plots for; (a) Cu-SG-*p*-NP and (b) Cu-SG-H<sub>2</sub>O<sub>2</sub> systems at different temperatures; 298, 303, and 308 K. (c) The corresponding Van't Hoff plot for the interaction of Cu-SG-*p*-NP and Cu-SG-H<sub>2</sub>O<sub>2</sub> systems at 298, 303, and 308 K.





## 4 Conclusion

This study demonstrates the potential of a facile acid-etching technique as a strategy for tuning the physicochemical properties of nanomaterials and endowing them with multifunctional applications. The prepared, ultrasmall Cu-SG (with an average size of 1 nm) achieved a 98% conversion of *p*-nitrophenol to *p*-aminophenol within six minutes and retained over 90% efficiency across five cycles, demonstrating excellent recyclability. As a colorimetric probe for H<sub>2</sub>O<sub>2</sub> detection, Cu-SG exhibited high specificity and a wide detection range. These findings establish Cu-SG as a promising candidate for environmental remediation and analytical sensing applications. The versatility of Cu-SG, combined with its ability to undergo facile acid-etching transformations, offers an innovative approach for developing efficient, stable, and recyclable water-soluble copper nanoclusters for both environmental and analytical uses.

## Data availability

The data supporting this article have been included as part of the ESI.†

## Conflicts of interest

There are no conflicts to declare.

## Acknowledgements

This work was supported by the National Natural Science Foundation of China (U23A2090), and the financial support from Department of Education of Anhui Province (2023AH010002); Mayowa Oyebanji would like to thank the China Scholarship Council of the Chinese government for the fellowship received.

## References

- 1 A. Baghdasaryan and T. Bürgi, Copper nanoclusters: designed synthesis, structural diversity, and multiplatform applications, *Nanoscale*, 2021, 13(13), 6283–6340, DOI: [10.1039/d0nr08489a](#).
- 2 X. Kang, Y. Li, M. Zhu and R. Jin, Atomically precise alloy nanoclusters: syntheses, structures, and properties, *Chem. Soc. Rev.*, 2020, 49(17), 6443–6514, DOI: [10.1039/c9cs00633h](#).
- 3 Y. Xue, Z. Cheng, M. Luo, H. Hu and C. Xia, Synthesis of Copper Nanocluster and Its Application in Pollutant Analysis, *Biosensors*, 2021, 11(11), 424, DOI: [10.3390/bios11110424](#).
- 4 M. Lettieri, P. Palladino, S. Scarano and M. Minunni, Copper nanoclusters and their application for innovative fluorescent detection strategies: An overview, *Sens. Actuators Rep.*, 2022, 4, 100108, DOI: [10.1016/j.snr.2022.100108](#).
- 5 C. Wang, C. Wang, L. Xu, H. Cheng, Q. Lin and C. Zhang, Protein-directed synthesis of pH-responsive red fluorescent copper nanoclusters and their applications in cellular imaging and catalysis, *Nanoscale*, 2014, 6(3), 1775–1781, DOI: [10.1039/c3nr04835g](#).
- 6 Y. Wu, C. Liu, C. Wang, Y. Yu, Y. Shi and B. Zhang, Converting copper sulfide to copper with surface sulfur for electrocatalytic alkyne semi-hydrogenation with water, *Nat. Commun.*, 2021, 12(1), 3881, DOI: [10.1038/s41467-021-24059-y](#).
- 7 T. Kou, C. Si, Y. Gao, J. Frenzel, H. Wang, X. Yan, Q. Bai, G. Eggeler and Z. Zhang, Large-scale synthesis and catalytic activity of nanoporous Cu–O system towards CO oxidation, *RSC Adv.*, 2014, 4(110), 65004–65011, DOI: [10.1039/c4ra12227e](#).
- 8 R. Mittal and N. Gupta, pH-dependent Synthesis and Interactions of Fluorescent L-Histidine Capped Copper Nanoclusters with Metal Ions, *J. Fluoresc.*, 2023, 34(5), 2085–2092, DOI: [10.1007/s10895-023-03433-7](#).
- 9 K. Anusuyadevi, S. P. Wu and S. Velmathi, Reversible enhancement of fluorescence in acidic pH driven by tryptophan stabilized copper nanoclusters and its application in bioimaging, *J. Photochem. Photobiol., A*, 2021, 421, 113526, DOI: [10.1016/j.jphotochem.2021.113526](#).
- 10 S. Basu, A. Paul and R. Antoine, Controlling the Chemistry of Nanoclusters: From Atomic Precision to Controlled Assembly, *Nanomaterials*, 2021, 12(1), 62, DOI: [10.3390/nano12010062](#).
- 11 Y. Peng, L. Shang, Y. Cao, G. I. N. Waterhouse, C. Zhou, T. Bian, L.-Z. Wu, C.-H. Tung and T. Zhang, Copper(i) cysteine complexes: efficient earth-abundant oxidation co-catalysts for visible light-driven photocatalytic H<sub>2</sub> production, *Chem. Commun.*, 2015, 51(63), 12556–12559, DOI: [10.1039/c5cc04739k](#).
- 12 M. Xu, R. Zhao, B. Liu, F. Geng, X. Wu, F. Zhang, R. Shen, H. Lin, L. Feng and P. Yang, Ultrasmall copper-based nanoplateforms for NIR-II light-triggered photothermal/photodynamic and amplified nanozyme catalytic therapy of hypoxic tumor, *Chem. Eng. J.*, 2024, 491, 151776, DOI: [10.1016/j.cej.2024.151776](#).
- 13 J. Ye, C. Li, X. Yao, M. Jin and D. Wan, Customizing a Hyperbranched Ligand Confers Supported Platinum Nanoclusters with Unexpected Catalytic Activity toward the Reduction of 4-Nitrophenol, *Langmuir*, 2023, 39(49), 18093–18100, DOI: [10.1021/acs.langmuir.3c02884](#).
- 14 X. Yao, R. Teng, M. Jin and D. Wan, Dendritic Molecular Template Mediates and Directs Self-Assembly of Uniform Gold Nanoclusters to One-Pot Afford 3D-Supported Active Catalysts, *ACS Appl. Polym. Mater.*, 2023, 5(9), 6842–6850, DOI: [10.1021/acsapm.3c00842](#).
- 15 Y. Huang, H. Zhong, C. Jiang, J. Yang, J. Zhang, F. Zhao and C. Liu, Copper-based nanomaterials as peroxidase candidates for intelligent colorimetric detection and antibacterial applications, *Particuology*, 2024, 84, 126–135, DOI: [10.1016/j.partic.2023.03.009](#).
- 16 A. Han, Y. Zhao, J. Wu, J. Guo and J. Xv, Self-assembled copper nanoclusters used to mimic peroxidase for glucose detection, *RSC Adv.*, 2024, 14(5), 3261–3266, DOI: [10.1039/d3ra07598b](#).



- 17 X. Sun, B. Yan, X. Gong, Q. Xu, Q. Guo and H. Shen, Eight-Electron Copper Nanoclusters for Photothermal Conversion, *Chem.-Eur. J.*, 2024, **30**(28), e202400527, DOI: [10.1002/chem.202400527](https://doi.org/10.1002/chem.202400527).
- 18 H. Wu, R. Anumula, G. N. Andrew and Z. Luo, A stable superatomic Cu<sub>6</sub>(SMPP)<sub>6</sub> nanocluster with dual emission, *Nanoscale*, 2023, **15**(8), 4137–4142, DOI: [10.1039/d2nr07223h](https://doi.org/10.1039/d2nr07223h).
- 19 K. B. Busi, S. Das, M. Palanivel, K. K. Ghosh, B. Gulyás, P. Padmanabhan and S. Chakraborty, Surface Ligand Influences the Cu Nanoclusters as a Dual Sensing Optical Probe for Localized pH Environment and Fluoride Ion, *Nanomaterials*, 2023, **13**(3), 529, DOI: [10.3390/nano13030529](https://doi.org/10.3390/nano13030529).
- 20 C. Zhang, W.-D. Si, Z. Wang, A. Dinesh, Z.-Y. Gao, C.-H. Tung and D. Sun, Solvent-Mediated Hetero/Homo-Phase Crystallization of Copper Nanoclusters and Superatomic Kernel-Related NIR Phosphorescence, *J. Am. Chem. Soc.*, 2024, **146**(15), 10767–10775, DOI: [10.1021/jacs.4c00881](https://doi.org/10.1021/jacs.4c00881).
- 21 S. I. Bukhari, M. M. Hamed, M. H. Al-Agamy, H. S. S. Gazwi, H. H. Radwan, A. M. Youssif and S. Ali, Biosynthesis of Copper Oxide Nanoparticles Using *Streptomyces* MHM38 and Its Biological Applications, *J. Nanomater.*, 2021, **2021**, 1–16, DOI: [10.1155/2021/6693302](https://doi.org/10.1155/2021/6693302).
- 22 M. A. Ben Aissa, B. Tremblay, A. Andrieux-Ledier, E. Maisonhaute, N. Raouafi and A. Courty, Copper nanoparticles of well-controlled size and shape: a new advance in synthesis and self-organization, *Nanoscale*, 2015, **7**(7), 3189–3195, DOI: [10.1039/c4nr06893a](https://doi.org/10.1039/c4nr06893a).
- 23 S. Qi, H. Saad Al-mashriqi, A. Salah and H. Zhai, Glutathione capped gold nanoclusters-based fluorescence probe for highly sensitive and selective detection of transferrin in serum, *Microchem. J.*, 2022, **175**, 107163, DOI: [10.1016/j.microc.2021.107163](https://doi.org/10.1016/j.microc.2021.107163).
- 24 R. Rajamanikandan and M. Ilanchelian, Highly selective and sensitive biosensing of dopamine based on glutathione coated silver nanoclusters enhanced fluorescence, *New J. Chem.*, 2017, **41**(24), 15244–15250, DOI: [10.1039/c7nj03170j](https://doi.org/10.1039/c7nj03170j).
- 25 F. Kalhori, H. Yazdyani, F. Khademorezaeian, N. Hamzkanloo, P. Mokaberi, S. Hosseini and J. Chamani, Enzyme activity inhibition properties of new cellulose nanocrystals from *Citrus medica* L. pericarp: A perspective of cholesterol lowering, *Luminescence*, 2022, **37**(11), 1836–1845, DOI: [10.1002/bio.4360](https://doi.org/10.1002/bio.4360).
- 26 Y. Luo, H. Miao and X. Yang, Glutathione-stabilized Cu nanoclusters as fluorescent probes for sensing pH and vitamin B1, *Talanta*, 2015, **144**, 488–495, DOI: [10.1016/j.talanta.2015.07.001](https://doi.org/10.1016/j.talanta.2015.07.001).
- 27 T. Jia, J. Ai, X. Li, M.-M. Zhang, Y. Hua, Y.-X. Li, C.-F. Sun, F. Liu, R.-W. Huang, Z. Wang, *et al.*, Atomically precise copper clusters with dual sites for highly chemoselective and efficient hydroboration, *Nat. Commun.*, 2024, **15**(1), 9551, DOI: [10.1038/s41467-024-53950-7](https://doi.org/10.1038/s41467-024-53950-7).
- 28 L. Wang, H. Liu, J. Zhuang and D. Wang, Small-Scale Big Science: From Nano- to Atomically Dispersed Catalytic Materials, *Small Sci.*, 2022, **2**(11), 2200036, DOI: [10.1002/smssc.202200036](https://doi.org/10.1002/smssc.202200036).
- 29 Y.-M. Wang, F.-Q. Yan, Q.-Y. Wang, C.-X. Du, L.-Y. Wang, B. Li, S. Wang and S.-Q. Zang, Single-atom tailored atomically-precise nanoclusters for enhanced electrochemical reduction of CO<sub>2</sub>-to-CO activity, *Nat. Commun.*, 2024, **15**(1), 1843, DOI: [10.1038/s41467-024-46098-x](https://doi.org/10.1038/s41467-024-46098-x).
- 30 Q. Yao, M. Zhu, Z. Yang, X. Song, X. Yuan, Z. Zhang, W. Hu and J. Xie, Molecule-like synthesis of ligand-protected metal nanoclusters, *Nat. Rev. Mater.*, 2025, **10**, 89–108, DOI: [10.1038/s41578-024-00741-7](https://doi.org/10.1038/s41578-024-00741-7).
- 31 H. Li, T. Liu, P. Wei, L. Lin, D. Gao, G. Wang and X. Bao, High-Rate CO<sub>2</sub> Electroreduction to C<sub>2</sub><sup>+</sup> Products over a Copper-Copper Iodide Catalyst, *Angew. Chem., Int. Ed.*, 2021, **60**(26), 14329–14333, DOI: [10.1002/anie.202102657](https://doi.org/10.1002/anie.202102657).
- 32 P. Liu and E. J. M. Hensen, Highly Efficient and Robust Au/MgCuCr<sub>2</sub>O<sub>4</sub> Catalyst for Gas-Phase Oxidation of Ethanol to Acetaldehyde, *J. Am. Chem. Soc.*, 2013, **135**(38), 14032–14035, DOI: [10.1021/ja406820f](https://doi.org/10.1021/ja406820f).
- 33 Y. Zhong, Y. Gu, L. Yu, G. Cheng, X. Yang, M. Sun and B. He, APTES-functionalized Fe<sub>3</sub>O<sub>4</sub> microspheres supported Cu atom-clusters with superior catalytic activity towards 4-nitrophenol reduction, *Colloids Surf., A*, 2018, **547**, 28–36, DOI: [10.1016/j.colsurfa.2018.03.015](https://doi.org/10.1016/j.colsurfa.2018.03.015).
- 34 J. Li, Y. Ren, F. Ji and B. Lai, Heterogeneous catalytic oxidation for the degradation of p -nitrophenol in aqueous solution by persulfate activated with CuFe<sub>2</sub>O<sub>4</sub> magnetic nano-particles, *Chem. Eng. J.*, 2017, **324**, 63–73, DOI: [10.1016/j.cej.2017.04.104](https://doi.org/10.1016/j.cej.2017.04.104).
- 35 C. Chu, S. Rao, Z. Ma and H. Han, Copper and cobalt nanoparticles doped nitrogen-containing carbon frameworks derived from CuO-encapsulated ZIF-67 as high-efficiency catalyst for hydrogenation of 4-nitrophenol, *Appl. Catal., B*, 2019, **256**, 117792, DOI: [10.1016/j.apcatb.2019.117792](https://doi.org/10.1016/j.apcatb.2019.117792).
- 36 S. K. Peng, H. Yang, D. Luo, G. H. Ning and D. Li, A Highly NIR Emissive Cu<sub>16</sub>Pd<sub>1</sub> Nanocluster, *Small*, 2023, **20**(13), 2306863, DOI: [10.1002/smll.202306863](https://doi.org/10.1002/smll.202306863).
- 37 A. Akhuli, A. Mahanty, D. Chakraborty, J. R. Biswal and M. Sarkar, Ligand-Mediated Surface Restructuring of Copper Nanoclusters and Its Impact on the Reduction of 4-Nitrophenol to 4-Aminophenol, *J. Phys. Chem. C*, 2024, **128**(37), 15380–15392, DOI: [10.1021/acs.jpcc.4c03529](https://doi.org/10.1021/acs.jpcc.4c03529).
- 38 H. Xiang, R. Cheng, C. Ruan, C. Meng, Y. Gan, W. Cheng, Y. Zhao, C.-Q. Xu, J. Li and C. Yao, A homologous series of macrocyclic Ni clusters: synthesis, structures, and catalytic properties, *Nanoscale*, 2024, **16**(9), 4563–4570, DOI: [10.1039/d3nr06015b](https://doi.org/10.1039/d3nr06015b).
- 39 B. Yan, X. You, X. Tang, J. Sun, Q. Xu, L. Wang, Z.-J. Guan, F. Li and H. Shen, Carboxylate-Protected “Isostructural” Cu<sub>20</sub> Nanoclusters as a Model System: Carboxylate Effect on Controlling Catalysis, *Chem. Mater.*, 2024, **36**(2), 1004–1012, DOI: [10.1021/acs.chemmater.3c03131](https://doi.org/10.1021/acs.chemmater.3c03131).
- 40 Z. Ding, X. Gao, Y. Yang, H. Wei, S. Yang and J. Liu, Amorphous copper(II)-cyanoimidazole frameworks as peroxidase mimics for hydrogen sulfide assay, *J. Colloid Interface Sci.*, 2023, **652**, 1889–1896, DOI: [10.1016/j.jcis.2023.09.014](https://doi.org/10.1016/j.jcis.2023.09.014).



- 41 X. Huang, F. Xia and Z. Nan, Fabrication of FeS<sub>2</sub>/SiO<sub>2</sub> Double Mesoporous Hollow Spheres as an Artificial Peroxidase and Rapid Determination of H<sub>2</sub>O<sub>2</sub> and Glutathione, *ACS Appl. Mater. Interfaces*, 2020, **12**(41), 46539–46548, DOI: [10.1021/acsami.0c12593](https://doi.org/10.1021/acsami.0c12593).
- 42 C. Zhang and Z. Nan, 2D/3D-Shaped Fe<sub>0.8</sub>Ni<sub>0.2</sub>S<sub>2</sub>/ZIF-67 as a Nanozyme for Rapid Measurement of H<sub>2</sub>O<sub>2</sub> and Ascorbic Acid with a Low Limit of Detection, *Inorg. Chem.*, 2022, **61**(35), 13933–13943, DOI: [10.1021/acs.inorgchem.2c01925](https://doi.org/10.1021/acs.inorgchem.2c01925).
- 43 Q. Liu, Q. Jia, R. Zhu, Q. Shao, D. Wang, P. Cui and J. Ge, 5,10,15,20-Tetrakis(4-carboxyl phenyl)porphyrin–CdS nanocomposites with intrinsic peroxidase-like activity for glucose colorimetric detection, *Mater. Sci. Eng., C*, 2014, **42**, 177–184, DOI: [10.1016/j.msec.2014.05.019](https://doi.org/10.1016/j.msec.2014.05.019).
- 44 P. Liu, M. Liang, Z. Liu, H. Long, H. Cheng, J. Su, Z. Tan, X. He, M. Sun, X. Li, *et al.*, Facile green synthesis of wasted hop-based zinc oxide nanozymes as peroxidase-like catalysts for colorimetric analysis, *Nanoscale*, 2024, **16**(2), 913–922, DOI: [10.1039/d3nr04336c](https://doi.org/10.1039/d3nr04336c).
- 45 B. Liu, H. Ruan, C. Li, J. Yao, B. Wei, L. Wang, S. Ban and J. Xie, Ce-doped indium oxide nanozymes with peroxidase-like activity induced by cerium–indium synergy for colourimetric detection of H<sub>2</sub>O<sub>2</sub>, *New J. Chem.*, 2023, **47**(39), 18476–18484, DOI: [10.1039/d3nj02985a](https://doi.org/10.1039/d3nj02985a).
- 46 L. Zhang, X. Hai, C. Xia, X.-W. Chen and J.-H. Wang, Growth of CuO nanoneedles on graphene quantum dots as peroxidase mimics for sensitive colorimetric detection of hydrogen peroxide and glucose, *Sens. Actuators, B*, 2017, **248**, 374–384, DOI: [10.1016/j.snb.2017.04.011](https://doi.org/10.1016/j.snb.2017.04.011).
- 47 H. Zhu, J. Deng, S. Mu, S. Xiao, Q. Li, W. Wang, Y. Gao, X. Luo, S. Gao and C. Cheng, Creating peroxidase-mimetic clusterzymes for efficient and selectively enzymatic diagnosis of biomarkers, *Chem. Eng. J.*, 2023, **462**, 142215, DOI: [10.1016/j.cej.2023.142215](https://doi.org/10.1016/j.cej.2023.142215).
- 48 X. Yuan, H. Zhao, Y. Yuan, M. Chen, L. Zhao and Z. Xiong, CuCo<sub>2</sub>S<sub>4</sub> nanozyme-based stimulus-responsive hydrogel kit for rapid point-of-care testing of uric acid, *Microchim. Acta*, 2022, **189**(8), 283, DOI: [10.1007/s00604-022-05381-8](https://doi.org/10.1007/s00604-022-05381-8).
- 49 P. Wang, L. Wen, C. Dong, L. Lin, C. Yang and X.-y. Li, Iron-molybdenum bimetal incorporated montmorillonite-based catalytic ceramic membrane for heterogenous Fenton reaction towards the degradation of micropollutants in water, *Chem. Eng. J.*, 2024, **500**, 156833, DOI: [10.1016/j.cej.2024.156833](https://doi.org/10.1016/j.cej.2024.156833).
- 50 K. Xiong, Z. Liu, L. Ren, D. Li, K. Dong, L. Yang and X. N. Zhang, N and O dual-doped porous carbon transformed from graphitic carbon nitride as a peroxydisulfate activator for tetracycline hydrochloride degradation, *New J. Chem.*, 2025, **49**, 855–864, DOI: [10.1039/d4nj04367g](https://doi.org/10.1039/d4nj04367g).
- 51 N. Wang, Z. Zhou, C. Liu, Y. Liu, X. Li, Y. Yang and L. Zhao, Intracellular and extracellular organic matter removal by BT/C heterogeneous interface under visible light photodriven, *Chem. Eng. J.*, 2024, **500**, 156727, DOI: [10.1016/j.cej.2024.156727](https://doi.org/10.1016/j.cej.2024.156727).
- 52 T. Wu, Z. Hu, J. Yang, Y. Jia, Z. Dong, Y. Tang and Y. Zhang, Insight into the roles of Cl<sup>−</sup> for the degradation of Acid Red 14 in an electrochemical advanced oxidation system: Mechanisms and DFT studies, *Chem. Eng. J.*, 2025, **503**, 158079, DOI: [10.1016/j.cej.2024.158079](https://doi.org/10.1016/j.cej.2024.158079).
- 53 Y. Li, Z. Kang, L. Kong, H. Shi, Y. Zhang, M. Cui and D.-P. Yang, MXene–Ti<sub>3</sub>C<sub>2</sub>/CuS nanocomposites: Enhanced peroxidase-like activity and sensitive colorimetric cholesterol detection, *Mater. Sci. Eng., C*, 2019, **104**, 110000, DOI: [10.1016/j.msec.2019.110000](https://doi.org/10.1016/j.msec.2019.110000).
- 54 R. Zhang, Y.-W. Mao, J.-Q. Li, L.-J. Ni, L. Lin, A.-J. Wang, J.-J. Feng, T. Y. Cheang and H. Zhou, Fe single atoms encapsulated in N, P-codoped carbon nanosheets with enhanced peroxidase-like activity for colorimetric detection of methimazole, *Spectrochim. Acta, Part A*, 2024, **310**, 123934, DOI: [10.1016/j.saa.2024.123934](https://doi.org/10.1016/j.saa.2024.123934).
- 55 T. Zhang, H. Li, M. Liu, H. Zhou, Z. Zhang, C. Yu, C. Wang and G. Wang, Improved the specificity of peroxidase-like carbonized polydopamine nanotubes with high nitrogen doping for glutathione detection, *Sens. Actuators, B*, 2021, **341**, 129987, DOI: [10.1016/j.snb.2021.129987](https://doi.org/10.1016/j.snb.2021.129987).
- 56 H. Yu, H. Wu, X. Tian, Y. Zhou, C. Ren and Z. Wang, A nano-sized Cu-MOF with high peroxidase-like activity and its potential application in colorimetric detection of H<sub>2</sub>O<sub>2</sub> and glucose, *RSC Adv.*, 2021, **11**(43), 26963–26973, DOI: [10.1039/d1ra04877e](https://doi.org/10.1039/d1ra04877e).
- 57 Q. Liu, S. Cao, Q. Sun, C. Xing, W. Gao, X. Lu, X. Li, G. Yang, S. Yu and Y. Chen, A perylenediimide modified SiO<sub>2</sub>@TiO<sub>2</sub> yolk-shell light-responsive nanozyme: Improved peroxidase-like activity for H<sub>2</sub>O<sub>2</sub> and sarcosine sensing, *J. Hazard. Mater.*, 2022, **436**, 129321, DOI: [10.1016/j.jhazmat.2022.129321](https://doi.org/10.1016/j.jhazmat.2022.129321).
- 58 D. Uzunoğlu and A. Özer, Colorimetric detection of H<sub>2</sub>O<sub>2</sub> by peroxidase-like catalyst iron-based nanoparticles synthesized by using hyperaccumulator plant-derived metal solution, *J. Environ. Chem. Eng.*, 2023, **11**(1), 109159, DOI: [10.1016/j.jece.2022.109159](https://doi.org/10.1016/j.jece.2022.109159).
- 59 H. Ye, Y. Ding, T. Liu, J. Li, Q. Wang, Y. Li, J. Gu, Z. Zhang and X. Wang, Colorimetric assay based on NiCo<sub>2</sub>S<sub>4</sub>@N,S-rGO nanozyme for sensitive detection of H<sub>2</sub>O<sub>2</sub> and glucose in serum and urine samples, *RSC Adv.*, 2022, **12**(32), 20838–20849, DOI: [10.1039/d2ra03444a](https://doi.org/10.1039/d2ra03444a).
- 60 L. F. M. Mazzini, A. C. Martins, K. L. A. d. Oliveira, R. S. de Oliveira and R. P. L. Moreira, Eco-friendly quantification of hydrogen peroxide in milk using green-synthesized iron nanoenzymes, *J. Food Compos. Anal.*, 2024, **135**, 106633, DOI: [10.1016/j.jfca.2024.106633](https://doi.org/10.1016/j.jfca.2024.106633).
- 61 A. Sharifi-Rad, J. Mehrzad, M. Darroudi, M. R. Saberi and J. Chamani, Oil-in-water nanoemulsions comprising Berberine in olive oil: biological activities, binding mechanisms to human serum albumin or holo-transferrin and QMMD simulations, *J. Biomol. Struct. Dyn.*, 2021, **39**(3), 1029–1043, DOI: [10.1080/07391102.2020.1724568](https://doi.org/10.1080/07391102.2020.1724568).
- 62 M. Kaffash, S. Tolou-Shikhzadeh-Yazdi, S. Soleimani, S. Hoseinpoor, M. R. Saberi and J. Chamani, Spectroscopy and molecular simulation on the interaction of Nano-Kaempferol prepared by oil-in-water with two carrier proteins: An investigation of protein-protein interaction,



- Spectrochim. Acta, Part A*, 2024, **309**, 123815, DOI: [10.1016/j.saa.2023.123815](#).
- 63 H. Monirinasab, M. Zakariazadeh, H. Kohestani, M. Kouhestani and F. Fathi, Study of  $\beta$ -lactam-based drug interaction with albumin protein using optical, sensing, and docking methods, *J. Biol. Phys.*, 2022, **48**(2), 177–194, DOI: [10.1007/s10867-021-09599-0](#).
- 64 X. Li and T. Ni, Probing the binding mechanisms of  $\alpha$ -tocopherol to trypsin and pepsin using isothermal titration calorimetry, spectroscopic, and molecular modeling methods, *J. Biol. Phys.*, 2016, **42**(3), 415–434, DOI: [10.1007/s10867-016-9415-6](#).
- 65 J. Chamani, H. Vahedian-Movahed and M. R. Saberi, Lomefloxacin promotes the interaction between human serum albumin and transferrin: A mechanistic insight into the emergence of antibiotic's side effects, *J. Pharm. Biomed. Anal.*, 2011, **55**(1), 114–124, DOI: [10.1016/j.jpba.2010.12.029](#).

